Received: 28 November 2023 | Revised: 9 January 2024 | Accepted: 18 January 2024 | Published online: 30 January 2024

RESEARCH ARTICLE

Journal of Optics and Photonics Research
2024, Vol. 1(2) 59–66
DOI: 10.47852/bonviewJOPR42022168

BON VIEW PUBLISHING

Investigation of Polymer-Based 1 × 2 All-Optical Switches at C-Band Wavelength

Md Koushik Alam[1], Noor Afsary[1], Md Zahidul Islam[1] and Md Omar Faruk Rasel[1,*]

[1]*Physics Discipline, Khulna University, Bangladesh*

Abstract: All-optical switches play a significant role in optical communication and signal processing using purely optical signals and offer efficient high-speed data transmission over conventional switches, which rely on optic–electronic conversions. This paper demonstrates 1 × 2 all-optical switches realized with the Mach–Zehnder interferometer (MZI) and directional couplers (DCs) for next-generation high-speed computing systems. We numerically design and simulate this optical switch by using the commercially available RSoft CAD BeamPROP solver. The proposed switches leverage the combined influence of DCs to achieve precise control over switching states by demonstrating remarkable phase-shifting properties with phase differences of $\frac{4\pi}{3}$ *and* $\frac{\pi}{2}$ between the MZI and DC. The optical switch exhibits excess losses (ELs) from 1.27 dB to 1.40 dB and crosstalk ranging from −13.303 dB to −11.034 dB in a wavelength range of 1.53–1.56 μm, and minimal EL and crosstalk are 1.27 dB and −13.303 dB at 1.55 μm. The proposed polymer-based 1 × 2 all-optical switches could be novel devices in high-speed data transmission for optical circuitry.

Keywords: all-optical switches, Mach–Zehnder interferometer, multimode interference waveguides, directional couplers, polymer waveguides, phase-shifting properties

1. Introduction

In today's world, we deal with vast amounts of data and advanced 5G networks. Optical communication systems are adjusting to handle the growing volume of information transmitted through these networks more efficiently. This adaptation is crucial for ensuring smooth and effective data transmission [1, 2]. However, there is a limit called the Shannon limit, which defines the maximum data for any communication channel, including optical systems [3]. This limit sets a boundary, guiding our efforts to enhance optical communication technologies. These days, the C-Band wavelength is a promising option for optical communication [4]. The C-Band is unique in optical transmission due to its lower signal loss. This characteristic allows signals to travel longer distances with minimal loss. Additionally, it supports multiple communication channels, making high-capacity data transmission easier [5]. Moreover, the C-Band demonstrates resilience against different interference sources. It efficiently tackles nonlinear effects, ensuring a stable and dependable propagation of signals [6]. These characteristics make the C-Band the preferred choice for telecommunications applications. It works exceptionally well, especially in long-distance and high-capacity situations, surpassing other frequency bands.

All-optical switches are significant in optical telecommunication, particularly in signal routing and time division signal processing [7, 8]. In recent years, various configurations of optical switches have developed based on the physical switching mechanism, such as acoustic optic [9], thermo-optic [10], electro-optic [11], and electro-mechanical [12]. All-optical switches offer notable advantages by reducing power consumption and minimizing heat generation. This enhancement improves overall energy efficiency compared to electronic switches [13]. They also exhibit lower signal loss and improved transmission quality over longer distances. Moreover, all-optical switches transmit signals without the need for optic-to-electronic conversions. These conversions limit the versatility and transparency of the system and introduce errors to the signal [14]. The equipment used for these conversions is the primary cost in modern networks. Eliminating such modifications can substantially reduce the overall cost of the system [15]. To enable all-optical switch control, nonlinear media is required, and managing power consumption is crucial for making these functions possible.

Compared to other optical switches, the multimode interference (MMI)-based switches cover the following advantages: low loss, ultra-compact size, high stability, large fabrication tolerance, and increased feasibility for the integration on printed circuit boards (PCBs) [14]. Another crucial component in this optical switching device is the Mach–Zehnder interferometer (MZI), which splits the input field into two equal intensities, causing the interference to form two possible outputs [16]. Combining MMI and MZI enhances the performance of all-optical switches. When an MMI is implemented using an MZI structure, it can produce output fields in either output 1 or 2. Numerous MMI optical switches have been developed based on thermo-optic and electro-optic effects [17–19]. These switches use external energy to shift the light phase, enabling optical switching. Several research studies have explored nonlinear waveguide couplers for optical switching [20, 21]. A switch based on a control beam in a nonlinear coupler

*Corresponding author: Md Omar Faruk Rasel, Physics Discipline, Khulna University, Bangladesh. Email: ofr_ju@phy.ku.ac.bd

is demonstrated by Samir et al. [21]. The control beam occupies one of the input and output ports in this configuration. Hence, a distinct separation between control and input signals is essential for proper switching functionality. To overcome this limitation, researchers have proposed and fabricated several optical switches within a single MMI region [22–24]. Rodgers et al. [25] introduced an all-optical switch with a single MMI region. According to the authors, no subsequent reports on single MMI-based all-optical switching have emerged. Bahrami and Rostami [26] proposed a 1×8 all-optical switch using MMI. However, a detailed analysis exposed significant drawbacks in both structures. The issue arose because of the high-intensity control field coupled with the inputs upon entering the structure. After the switching operation, it was necessary to separate the control field from the input fields. This phenomenon introduced additional challenges in optical communication systems. To fix these problems, another well-known method involves switching with MZI-assisted MMI couplers, employing nonlinear directional couplers (DCs). In this approach, the DC functions as a phase controller. It needs different phases of light to switch between output ports. Recently, a switching method based on MZI utilizing MMI couplers or splitters has been demonstrated [14, 27, 28]. However, a significant challenge with these devices is the requirement for an extended length for effective switching. Consequently, these switches cannot be efficiently integrated into small chip areas. Additionally, the intensity of outputs during switching is non-uniformly distributed, resulting in varied losses among different outputs. This asymmetry means that one output performs better than the other.

To enhance the MZI-assisted MMI all-optical switch, it is important to ensure a consistent output in different switching states. Achieving symmetry in losses is crucial for better performance in both outputs during switching. In this context, polymer optical waveguides emerge as a promising technology for advancing these optical devices [29, 30]. Over the last decade, polymer waveguides have demonstrated significant advantages over traditional silicon counterparts, primarily due to their unique material properties. These properties include low propagation loss, easy integration of optical devices [31–33] with PCBs, and high flexibility.

This paper presents the 1×2 all-optical switch realized with organic–inorganic hybrid polymer materials, leveraging a MMI-assisted MZI configuration with DCs serving as phase shifters. In this design, we position the DCs at the two outermost arms within the inter-stage of MMI-based MZI couplers, assigning them the crucial role of phase shifters. The significance of the DCs lies in their ability to shift the phase between the symmetric arms of the MZI, effectively addressing the input phase difference between the MZI and DC. The main focus of this paper is to establish an individual phase control mechanism while ensuring no coupling with input and output ports. In addition, we aim to achieve a uniform intensity distribution between the two outputs, maintain the symmetric loss for both outputs, and ensure stability within the C-Band wavelength region.

2. Theory and Simulation Setup

The MMI devices follow the self-imaging principle, in which an input field profile is replicated in single or multiple images at regular intervals along the propagation direction of the multimode waveguides [34]. This property effectively manipulates and controls optical signals within the MMI devices. We denote the width of the MMI waveguide as W_{MMI} . The positions of the input and output ports are introduced as x_{pos}:

$$x_{pos} = \frac{W_{\mathrm{mmi}}}{5}, -\frac{W_{\mathrm{mmi}}}{5} \tag{1}$$

In the general interference case, the minimum length of the MMI coupler is defined as $L_{MMI} = L_{\pi}$, where L_{π} represents the half-beat length, which can be expressed as [34]:

$$L_{\pi} = \frac{\pi}{\beta_0 - \beta_1} \approx \frac{4 n_r W_e^2}{3\lambda_0} \tag{2}$$

where β_0 and β_1 represent the propagation constants, n_r denotes the refractive index of the core layer, W_e stands for the effective width of the MMI coupler, and λ_0 is the free space wavelength. The effective width, W_e, can be considered as the lateral penetration depth of each mode field, accounting to the Goos–Hänchen shifts at the ridge boundaries. Generally, the effective width, W_e, can be reasonably estimated using the approach proposed by Soldano and Pennings [34]:

$$W_e = W_{MMI} + \left(\frac{\lambda_0}{\pi}\right)\left(\frac{n_2}{\mathrm{n}_1}\right)^{2\sigma}(n_1^2 - n_2^2)^{-\frac{1}{2}} \tag{3}$$

where W_{MMI} is the width of MMI, n_2 and n_1 are the refractive index of cladding and core, respectively, and $\sigma = 0$ or 1, which depends on the polarization mode [35]. For a 1×2 MMI coupler, the optical relative phase signal at the output ports is given by Cooney and Peters [36]:

$$\left.\begin{array}{l} \phi_{xy} = \phi_0 + \pi + \frac{\pi}{4}(y - x)(2 - x - y) \ \text{ for } x + y \text{ even} \\ \phi_{xy} = \phi_0 + \frac{\pi}{4}(x + y - 1)(2 + x + y) \text{ for } x + y \text{ odd} \end{array}\right\} \tag{4}$$

where ϕ_0 is the initial phase, x is the number of the input waveguides, and y is the number of the output waveguides. In an all-optical switching setup, two nonlinear DCs, acting as phase shifters, are crucial for the device's structure, leveraging the Kerr effect [37]. These couplers consist of two closely positioned waveguides, allowing to form a coupling within a short distance, provided that one or both waveguides exhibit nonlinear behavior. This nonlinear property is induced by a high-intensity control field, which alters the refractive index. When the distance between the couplers is minimal, and the mode field amplitudes change gradually along the propagation direction, the interaction of electric fields in these couplers follows coupled mode equations, given below:

$$-i\frac{dA}{dz} = \alpha B + \beta_1(|F_a|^2 + 2|F_b|^2)A \tag{5}$$

$$-i\frac{dB}{dz} = \alpha A + \beta_2(|F_b|^2 + 2|F_a|^2)B \tag{6}$$

where α is the linear coupling coefficient, it is determined by $\alpha = \frac{\pi}{2L_c}$, L_C is the coupling length, F_a and F_b are field amplitudes of the control and signal waveguides of the DC, and β_1, β_2 are the nonlinear coefficients. When influenced by self-phase modulation in the nonlinear DC, the phase within the coupler can be altered in proportion to the intensity of the input electrical fields in the waveguides. The expression for these

nonlinear phase shifts in the directional coupling waveguides can be represented as follows:

$$\Delta\phi_{\text{Left}} = \frac{2\pi n_2 L_c (I_s + 2I_1)}{\lambda_0} \tag{7}$$

$$\Delta\phi_{\text{Right}} = \frac{2\pi n_2 L_c (I_s + 2I_2)}{\lambda_0} \tag{8}$$

Here, I_1 and I_2 represent the field intensities of the control signal in waveguides 1 and 2, respectively. Additionally, I_s corresponds to the signal's field intensity in the outermost arms of the waveguide.

We design and develop the MZI-assisted MMI optical switches by using the commercially available RSoft CAD BeamPROP solver. The RSoft CAD BeamPROP solver is handy for investigating light propagation, optimizing the parameters of the device, and analyzing the switching properties.

3. Design and Characterization

3.1. Structural design

The schematic of the proposed MMI and MZI-based SI optical switch is shown in Figure 1, and we use the RSoft CAD BeamPROP solver to design and simulate these devices. In the MZI, optical power undergoes splitting and combining before reaching the MMI waveguide with two outputs. This design seamlessly integrates an MMI structure with an MZI, featuring two DCs strategically placed on either side of the MMI and MZI-based model. These DCs play a pivotal role in manipulating the phase between the symmetric arms of the MZI by enabling control modulation of optical signals. We use an organic–inorganic hybrid polymer material combination: core NP001L2 (n_1 −1.573) and cladding NP-216 (n_1 −1.560) [38] for this modeling. The advantages of the organic–inorganic hybrid materials, named SUNCONNECT® provided by Nissan Chemical Co. Ltd., cover low absorption loss due to their structural bonding and high thermal resistivity in high temperature at 300 °C [39]. The organic–inorganic hybrid resign is the base material, and the product names vary depending on the refractive index and viscosities. The dimension of the waveguide is squared shaped, and the outputs from the MMI waveguide are placed 6.2 μm away from the MMI central point. Also, the separation gap between both DC outputs is 49 μm apart from the MMI central position, as shown in Figure 1(d). We can fabricate the schematic shown in Figure 1 by using the imprint technique, as demonstrated by Abe et al. [40]. A cladding monomer is initially applied onto a glass substrate inside the silicone frame. A polydimethyl-siloxane-based mold featuring the core patterns, known as the grooves, is employed on the cladding layer and the cure cladding monomer with UV exposure. Then, the grooves are filled with another liquid-state core monomer. Finally, we use the cladding monomer on the core layer to form an upper cladding layer, and the upper cladding monomer is cured by UV exposure followed by post-baking.

3.2. Cut-off core width for single-mode condition

The core width plays a pivotal role in characterizing the waveguide dimension. We investigate the cut-off core width for the material combination of NP-001L2 and NP-216 to satisfy single-mode conditions. The cut-off core width for the single-mode waveguide is shown in Figure 2, where the effective index varies as a function of waveguide width, including the fundamental mode (mode 0) and first-order mode (mode 1) at 1550 nm. From Figure 2(a), we confirm that the core width for the single-mode waveguide should be $\leq$ 6 μm at 1550 nm. We have investigated the performance of the waveguides based on the waveguide width, and we confirm that the maximum output intensity is obtained in the range of 4.5–6 μm, as shown in Figure 2(b). Thus, considering the single-mode condition and the performance, we set the core width of 5 μm for this switch.

Figure 1
Schematic design of the all-optical switch: (a) 3D view, (b) top view with parameter indications, (c) input cross-section, and (d) output cross-section

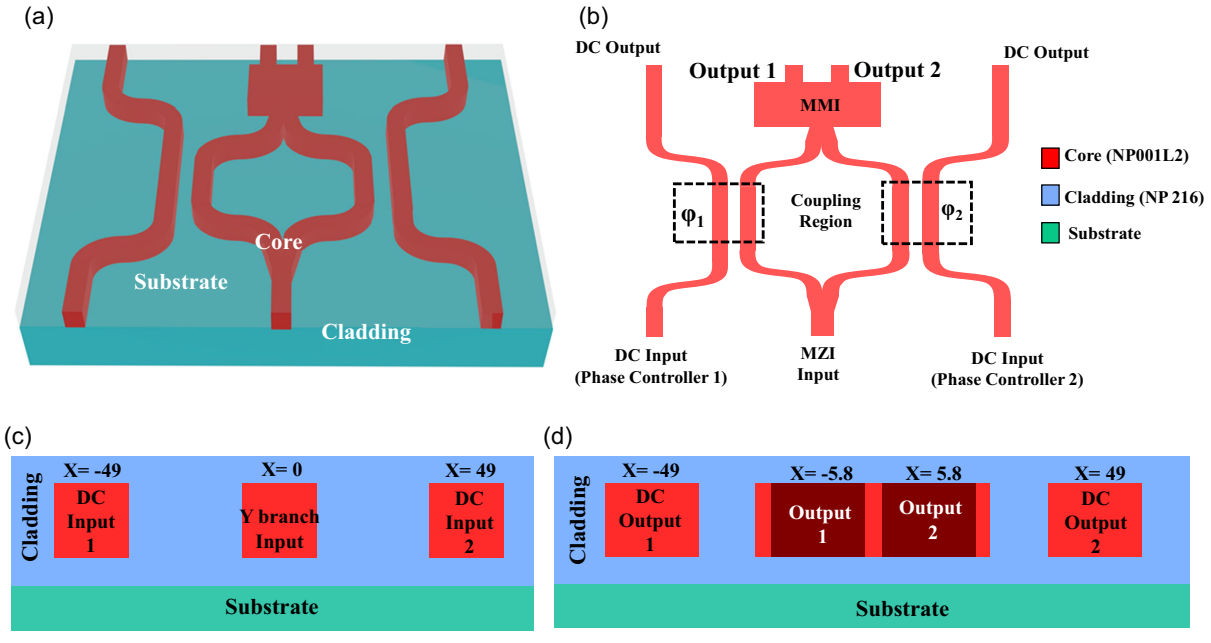

Figure 2
Core width optimization: (a) cut-off core width for single-mode condition and (b) optimized core width within single-mode condition

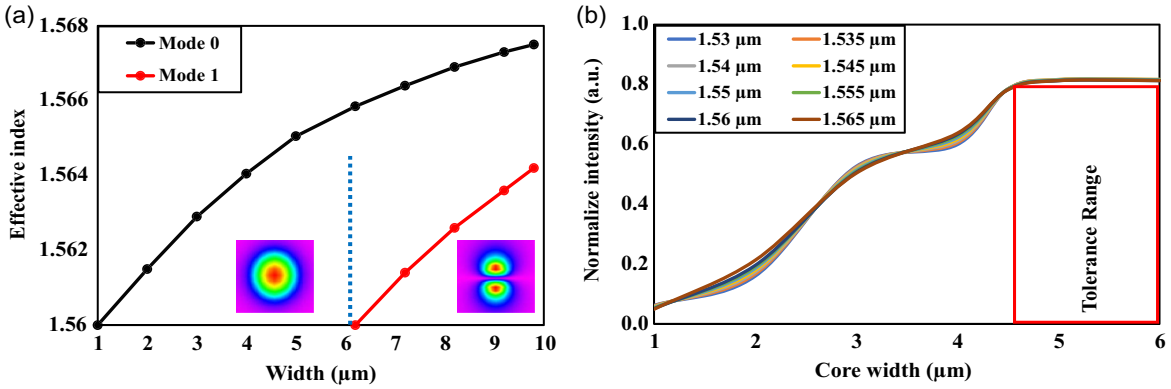

3.3. Optical switching property analysis

A phase shifter switch is a vital component for optical communication systems for precise modulation of the phase of optical signals. The manipulation of the light phase is essential for the applications, including signal processing, wavelength tuning, and optical switching. This investigation demonstrates the intricate integration of a phase shifter into a MZI structure, as illustrated in Figure 1. The MZI consists of two arms with an optical path difference, precisely adjusted by the integrated phase shifter. A phase shifter is designed to alter the phase of the signal, and a phase shifter (arms of DCs) can influence interference patterns or modulate the intensity of light by changing the phase of the input signal. As light traverses through the MZI, it undergoes interference, and the controlled manipulation of the phase difference between the arms of the MZI governs the output intensity. This capability facilitates the formation of constructive or destructive interference patterns, thereby influencing the routing of optical signals through the different paths.

Table 1 presents the parameters governing the phase-shifting properties between the two symmetric arms of the MZI. φ_1 and φ_2 denote the phases of phase controllers 1 and 2, respectively. Constructive interference occurs when the phase difference between the input and phase controller is set to $\frac{4\pi}{3}$. This condition facilitates light coupling into the MZI arm, and the result is obtained from output 2, where MMI occurs between the MMI. Conversely, when the phase difference between the output and phase controller is $\frac{\pi}{2}$, destructive interference occurs. As a result, light couples, and all the light passes through the DC port. The simulation results of this switching phenomenon are shown in Figure 3.

Table 1
The parameters of the phase-shifting property

Input light phase	φ_1	φ_2	Outputs
0	$\frac{4\pi}{3}$	$\frac{\pi}{2}$	Output 1 OFF Output 2 ON
0	$\frac{\pi}{2}$	$\frac{4\pi}{3}$	Output 1 ON Output 2 OFF

Figure 3(a) demonstrates that the constructive interference occurs between phase controller-1 and the left arm of the MZI, and the destructive interference occurs between the phase controller-2 and the right arm of the MZI. Following constructive interference (between phase controller-1 and the left arm of the MZI), light enters the left arm of the MZI. Then, upon reaching the MMI section, MMI occurs, which results in output 2 being in the ON state. Alternatively, for the destructive interferences (between the phase controller-2 and the right arm of the MZI), light enters into

Figure 3
Switching phenomena: (a) output 2 ON; output 1 OFF and (b) output 1 ON; output 2 OFF

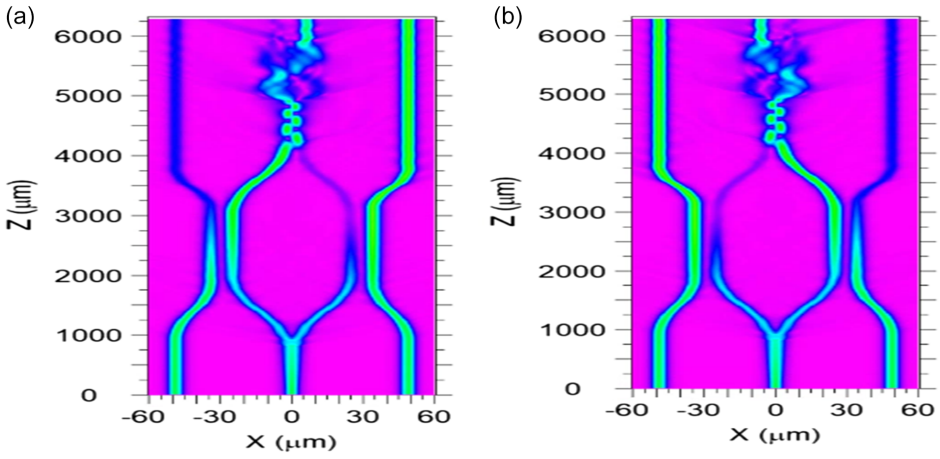

the phase controller-2, causing the right arm of the MZI to be devoid of light. Consequently, output 1 is in the OFF state. Figure 3(b) represents the inverse scenario of Figure 3(a). In Figure 3(b), constructive interference occurs between the phase controller-2 and the right arm of the MZI. Alternatively, destructive interference occurs between the phase controller-1 and the left arm of the MZI. Light enters into the right arm of the MZI through phase controller-2, leading to output 1 being in the ON state. Simultaneously, the left arm of the MZI contains no light at the end of destructive interference, leading to output 2 being in the OFF state.

We have investigated the normalized intensity between the two outputs of the MMI at the C-band wavelength region, as shown in Figure 4. In the RSoft CAD BeamPROP solver, the normalized launch power is 1 a.u. for a single launch field. As the number of launch fields increases, the launch power is distributed between the launch fields. This optical switch involves three launch fields: 2 for phase controllers 1 and 2, respectively, and the third one for the MZI input at 0.622 a.u. Hence, each MMI output initially carries 0.311 a.u. power. To identify the optimal condition of the switch, we examined the intensity of output 1 and output 2 in both the ON and OFF states, as presented in Figure 4(a), which reveals that the intensity for output 1 and output 2 is identical for both ON and OFF states due to the symmetric components of the device. Thus, the output results overlap each other for the ON and OFF states. In Figure 4(b), the intensity variation is measured when the phase difference between the phase controller-1 and left arm of the MZI is set to $\frac{\pi}{2}$, and the phase controller-2 and right arm of the MZI is set to $\frac{4\pi}{2}$ at C-band wavelength. Under these conditions, output 1 consistently remains in the ON state, with the intensity gradually increasing as the wavelength increases until 1.55 μm and starts decreasing again. And the intensity of output 2 is notably very small. Additionally, we measured the intensity variation when the phase difference between phase controller-1 and the left arm of the MZI is set to $\frac{4\pi}{2}$, and phase controller-2 and the right arm of the MZI is set to $\frac{\pi}{2}$, as illustrated in Figure 4(c), which shows that the output 2 is the ON state, and the intensity increases with the wavelength. The maximum intensity is obtained at 1.55 μm and starts to decrease very slowly. Similar to the previous case, the opposite output (output 1) exhibits minimal power, demonstrating an efficient switching phenomenon. This device is primarily optimized at 1.55 μm and is expanded into the C-Band region because minimal deviation occurs in this wavelength range. Since the device is optimized for 1.55 μm, it exhibits the maximum output intensity at 1.55 μm.

The separation gap between the MZI and the phase controller is very significant for light coupling phenomena. We investigate the tolerance range of the separation gap [41] between the MZI arm and the phase controller, as illustrated in Figure 5. We examine the intensity difference between the two outputs of the MMI based on the tolerance range of the separation gap. In this structure, functioning as a switch, we aim to activate only one output at a time, rendering the other output inactive. In Figure 4, we vary the separation gap between the phase controller and MZI from 7 to 11 μm, and we investigate the output intensity differences between the two outputs. This graph suggests that the tolerance region should be 8.2–9.2 μm, which fits the phase-shifting property well.

4. Loss Calculation

Loss calculation is crucial to investigate the efficiency and performance of optical devices. We calculate the excess loss (EL) and crosstalk of this optical switch by using the equations [42] as follows:

$$EL = -10\log 10\left(\frac{\sum_{i=1}^{n} P_{out}}{P_{in}}\right) \tag{9}$$

Figure 4
Intensity variation for C-band wavelength: (a) output 1 and output 2 are ON and OFF states, (b) output 1 is ON state, and (c) output 2 is ON state

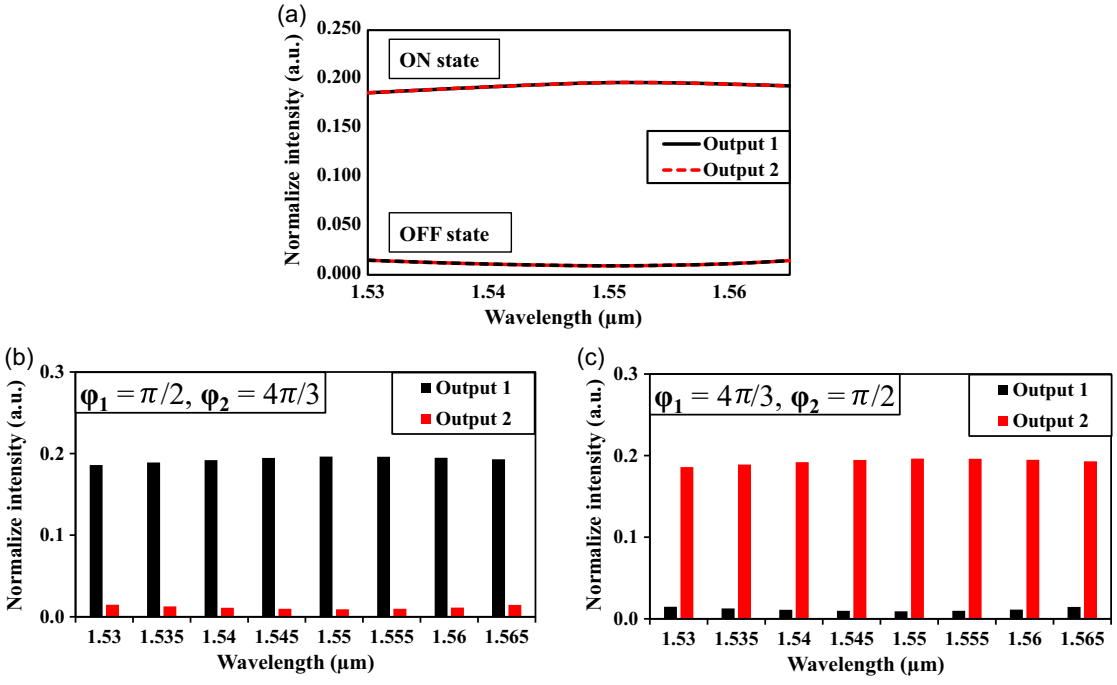

Figure 5
Analysis of the tolerance range of the separation gap

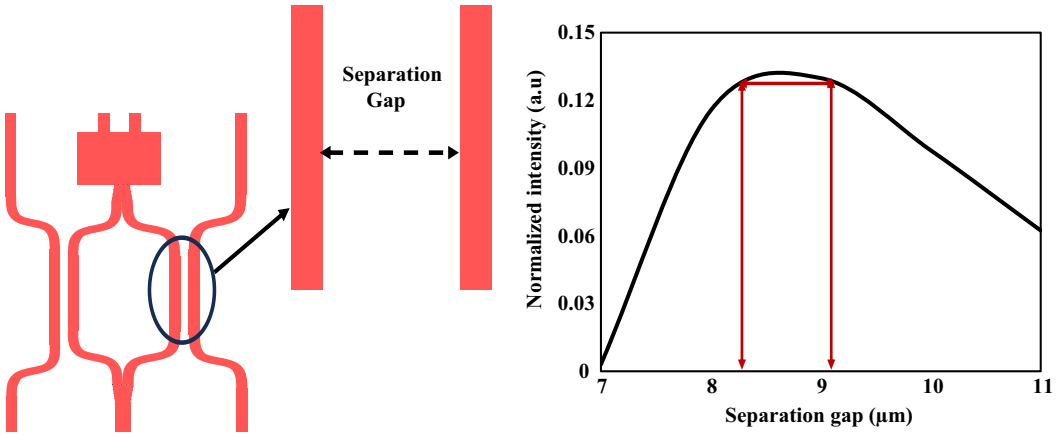

$$Crosstalk = 10log_{10}\left(\frac{P_{unwanted}}{P_{desired}}\right) \quad (10)$$

where P_{in} and P_{out} are the power of the input and output of these devices, and we calculate the EL for this optical switch by varying the wavelength, as shown in Figure 6. This figure illustrates the variation in EL with changing wavelengths within the C-Band range (1.53–1.565 μm). The black line represents the EL for output 1 when output 1 is in the ON and output 2 is in the OFF state. The red line represents the EL for output 2 when output 2 is in the ON state and output 1 is in the OFF state. Both outputs demonstrate that the ELs of the switch decrease from 1.53 μm to 1.55 μm and start to increase again. Minimal EL is obtained at 1.55 μm (1.27 dB), which is used as the primary optimized wavelength for the device.

Figure 6
Excess loss calculation as a function of wavelength

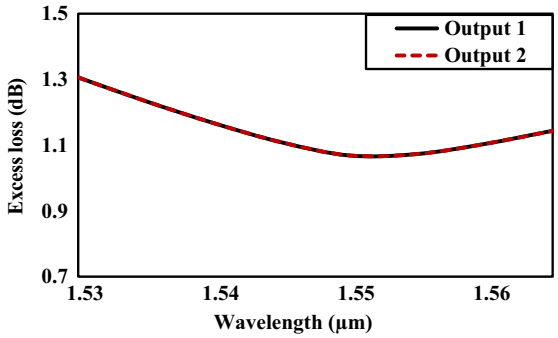

Crosstalk refers to the unwanted interference or coupling of signals between two or more channels or paths. Optical crosstalk occurs when the optical signals in one channel unintentionally influence or interfere with signals in another channel. We calculate the crosstalk of his device within the C-Band wavelength limit, as shown in Figure 7, and the crosstalk is lower than −13.303 dB at 1550 nm. This figure illustrates the variation in crosstalk with changing wavelengths across the C-Band

Figure 7
Crosstalk calculation in terms of wavelength

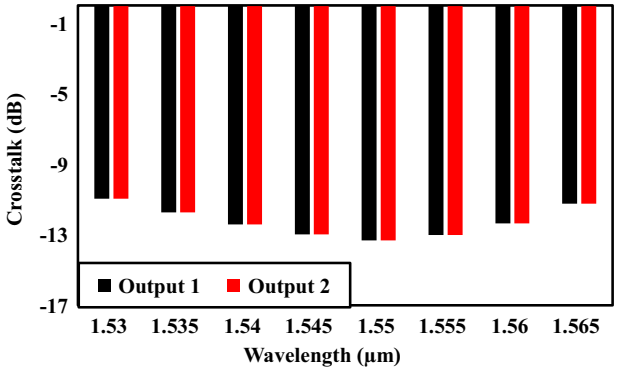

wavelength range, from 1.53 μm to 1.565 μm. The black line represents the crosstalk of output 1 when it is in the ON state, while the red line represents the crosstalk of output 2 in the ON state. The trend indicates that increasing the wavelength leads to a decrease in crosstalk for both outputs. However, when the wavelength crosses 1.55 μm, the crosstalk rises gradually, as the 1.55 μm wavelength is selected for primary optimization for this optical switch. This wavelength-dependent behavior is crucial in understanding and optimizing the performance of the optical system, particularly in scenarios where minimizing crosstalk is essential for reliable signal transmission.

5. Conclusion

We have demonstrated polymer-based all-optical switches incorporating the MZI and MMI with the DCs. This switch executes phase-shifting properties by combining the DCs. The results of this device include an impressive switching ability with a phase difference of $\frac{4\pi}{3}$ *and* $\frac{\pi}{2}$ between the MZI and DC. The switch exhibits minimal EL of 1.27 dB, and the crosstalk is −13.303 dB at 1.55 μm. Thus, the all-optical switches could be the novel devices for the high-performance photonic circuitry and these numerical demonstrations could give the guideline to fabricate the polymer all-optical switches.

Ethical Statement

This study does not contain any studies with human or animal subjects performed by any of the authors.

Conflicts of Interest

The authors declare that they have no conflicts of interest to this work.

Data Availability Statement

The data that support the findings of this study are openly available in Optica Open at https://doi.org/10.1364/opticaopen.24574615

References

[1] Doerr, C., & Chen, L. (2018). Silicon photonics in optical coherent systems. *Proceedings of the IEEE*, *106*(12), 2291–2301. https://doi.org/10.1109/JPROC.2018.2866391

[2] Shi, Y., Zhang, Y., Wan, Y., Yu, Y., Zhang, Y., Hu, X., . . . , & Pan, B. (2022). Silicon photonics for high-capacity data communications. *Photonics Research*, *10*(9), A106–A134. https://doi.org/10.1364/prj.456772

[3] Ellis, A. D., Zhao, J., & Cotter, D. (2010). Approaching the non-linear Shannon limit. *Journal of Lightwave Technology*, *28*(4), 423–433. https://doi.org/10.1109/JLT.2009.2030693

[4] Lopez, V., Zhu, B., Moniz, D., Costa, N., Pedro, J., Xu, X., . . . , & Sanders, S. (2020). Optimized design and challenges for C&L band optical line systems. *Journal of Lightwave Technology*, *38*(5), 1080–1091. https://doi.org/10.1109/JLT.2020.2968225

[5] Chen, Z., Wan, L., Gao, S., Zhu, K., Zhang, M., Li, Y., . . . , & Li, Z. (2022). On-chip waveguide amplifiers for multi-band optical communications: A review and challenge. *Journal of Lightwave Technology*, *40*(11), 3364–3373. https://doi.org/10.1109/JLT.2022.3153447

[6] Hraghi, A., Rizzelli, G., Pagano, A., Ferrero, V., & Gaudino, R. (2022). Analysis and experiments on C band 200G coherent PON based on Alamouti polarization-insensitive receivers. *Optics Express*, *30*(26), 46782–46797. https://doi.org/10.1364/oe.472470

[7] Willner, A. E., Khaleghi, S., Chitgarha, M. R., & Yilmaz, O. F. (2014). All-optical signal processing. *Journal of Lightwave Technology*, *32*(4), 660–680. https://doi.org/10.1109/JLT.2013.2287219

[8] Yan, L., Willner, A. E., Wu, X., Yi, A., Bogoni, A., Chen, Z. Y., & Jiang, H. Y. (2012). All-optical signal processing for ultrahigh speed optical systems and networks. *Journal of Lightwave Technology*, *30*(24), 3760–3770. https://doi.org/10.1109/JLT.2012.2205134

[9] Wu, Q., Gao, Z., Tian, X., Su, X., Li, G., Sun, Y., . . . , & Tao, X. (2017). Biaxial crystal β-$BaTeMo_2O_9$: Theoretical analysis and the feasibility as high-efficiency acousto-optic Q-switch. *Optics Express*, *25*(21), 24893–24900. https://doi.org/10.1364/oe.25.024893

[10] Zhou, T., Jia, H., Ding, J., Zhang, L., Fu, X., & Yang, L. (2018). On-chip broadband silicon thermo-optic 2 × 2 four-mode optical switch for optical space and local mode switching. *Optics Express*, *26*(7), 8375–8384. https://doi.org/10.1364/oe.26.008375

[11] van Campenhout, J., Green, W. M. J., & Vlasov, Y. A. (2009). Design of a digital, ultra-broadband electro-optic switch for reconfigurable optical networks-on-chip. *Optics Express*, *17*(26), 23793–23808. https://doi.org/10.1364/OE.17.023793

[12] Liu, T., Pagliano, F., & Fiore, A. (2017). Nano-opto-electro-mechanical switch based on a four-waveguide directional coupler. *Optics Express*, *25*(9), 10166–10176. https://doi.org/10.1364/oe.25.010166

[13] Nozaki, K., Tanabe, T., Shinya, A., Matsuo, S., Sato, T., Taniyama, H., & Notomi, M. (2010). Sub-femtojoule all-optical switching using a photonic-crystal nanocavity. *Nature Photonics*, *4*(7), 477–483. https://doi.org/10.1038/nphoton.2010.89

[14] Bahrami, A., Rostami, A., & Nazari, F. (2011). MZ-MMI-based all-optical switch using nonlinear coupled waveguides. *Optik*, *122*(20), 1787–1790. https://doi.org/10.1016/j.ijleo.2010.11.005

[15] Asobe, M. (1997). Nonlinear optical properties of chalcogenide glass fibers and their application to all-optical switching. *Optical Fiber Technology*, *3*(2), 142–148. https://doi.org/10.1006/ofte.1997.0214

[16] Bananej, A., & Li, C. (2004). Controllable all-optical switch using an EDF-ring coupled M-Z interferometer. *IEEE Photonics Technology Letters*, *16*(9), 2102–2104. https://doi.org/10.1109/LPT.2004.833054

[17] Al-Hetar, A. M., Mohammad, A. B., Supa'at, A. S. M., Shamsan, Z. A., & Yulianti, I. (2011). Fabrication and characterization of polymer thermo-optic switch based on MMI coupler. *Optics Communications*, *284*(5), 1181–1185. https://doi.org/10.1016/j.optcom.2010.10.025

[18] Gao, L., Sun, J., Sun, X., Li, T., Gao, W., Yan, Y., & Zhang, D. (2010). Simulation and optimization of a polymer 2 × 2 multimode interference-Mach Zehnder interferometer electro-optic switch with push-pull electrodes. *Optics & Laser Technology*, *42*(1), 85–92. https://doi.org/10.1016/j.optlastec.2009.05.002

[19] Xia, J., Yu, J., Wang, Z., Fan, Z., & Chen, S. (2004). Low power 2 × 2 thermo-optic SOI waveguide switch fabricated by anisotropy chemical etching. *Optics Communications*, *232*(1–6), 223–228. https://doi.org/10.1016/j.optcom.2003.12.074

[20] Fujisawa, T., & Koshiba, M. (2006). All-optical logic gates based on nonlinear slot-waveguide couplers. *Journal of the Optical Society of America B*, *23*(4), 684–691. https://doi.org/10.1364/JOSAB.23.000684

[21] Samir, W., Pask, C., & Garth, S. J. (1994). Signal switching by a control beam in a nonlinear coupler. *Journal of the Optical Society of America B*, *11*(11), 2193–2205. https://doi.org/10.1364/JOSAB.11.002193

[22] Jia, X., Luo, S., & Cheng, X. (2008). Design and optimization of novel ultra-compact SOI multimode interference optical switch. *Optics Communications*, *281*(5), 1003–1007. https://doi.org/10.1016/j.optcom.2007.10.074

[23] May-Arrioja, D. A., Bickel, N., & Likamwa, P. (2006). Robust 2 × 2 multimode interference optical switch. *Optical and Quantum Electronics*, *38*(7), 557–566. https://doi.org/10.1007/s11082-005-4699-y

[24] Yin, R., Teng, J., & Chua, S. (2008). A 1 × 2 optical switch using one multimode interference region. *Optics Communications*, *281*(18), 4616–4618. https://doi.org/10.1016/j.optcom.2008.05.042

[25] Rodgers, J. S., Ralph, S. E., & Kenan, R. P. (2000). Self-guiding multimode interference threshold switch. *Optics Letters*, *25*(23), 1717–1719. https://doi.org/10.1364/OL.25.001717

[26] Bahrami, A., & Rostami, A. (2011). A proposal for 1 × 8 all-optical switch using multimode interference. *Optica Applicata*, *41*(1), 165–172.

[27] Ghayour, R., Taheri, A. N., & Fathi, M. T. (2008). Integrated Mach-Zehnder-based 2 × 2 all-optical switch using nonlinear two-mode interference waveguide. *Applied Optics*, *47*(5), 632–638. https://doi.org/10.1364/AO.47.000632

[28] Yang, D., Li, Y., Sun, F., Chen, S., & Yu, J. (2005). Fabrication of a 4 × 4 strictly nonblocking SOI switch matrix. *Optics Communications*, *250*(1–3), 48–53. https://doi.org/10.1016/j.optcom.2005.02.008

[29] Alam, M. K., Afsary, N., Rasel, M. O. F., & Ishigure, T. (2021). Multimode interference based Y-branch polymer optical waveguide splitter: Design and investigation. In *International Conference on Electronics, Communications and Information Technology,* 1–4. https://doi.org/10.1109/ICECIT54077.2021.9641413

[30] Rasel, M. O. F., Afsary, N., Alam, M. K., Tasnim, F., Sakib, M. N., Hatai, R., & Ishigure, T. (2023). Step and graded-index core-based polymer multimode interference splitters for photonic integrated circuits. *Optik*, *290*, 171278. https://doi.org/10.1016/j.ijleo.2023.171278

[31] Dangel, R., Hofrichter, J., Horst, F., Jubin, D., La Porta, A., Meier, N., . . . , & Offrein, B. J. (2015). Polymer waveguides for electro-optical integration in data centers and high-performance computers. *Optics Express*, *23*(4), 4736–4750. https://doi.org/10.1364/oe.23.004736

[32] Jiang, L., Huang, Q., & Chiang, K. S. (2022). Low-power all-optical switch based on a graphene-buried polymer waveguide Mach-Zehnder interferometer. *Optics Express*, *30*(5), 6786–6797. https://doi.org/10.1364/oe.452075

[33] Song, Q. Q., Chen, K. X., & Hu, Z. F. (2020). Low-power broadband thermo-optic switch with weak polarization dependence using a segmented graphene heater. *Journal of Lightwave Technology*, *38*(6), 1358–1364. https://doi.org/10.1109/JLT.2019.2955511

[34] Soldano, L. B., & Pennings, E. C. M. (1995). Optical multi-mode interference devices based on self-imaging: Principles and applications. *Journal of Lightwave Technology*, *13*(4), 615–627. https://doi.org/10.1109/50.372474

[35] Gong, Z., Yin, R., Ji, W., & Wu, C. (2018). Semiconductor laser using multimode interference principle. *Optics & Laser Technology*, *98*, 75–78. https://doi.org/10.1016/j.optlastec.2017.06.029

[36] Cooney, K., & Peters, F. H. (2016). Analysis of multimode interferometers. *Optics Express*, *24*(20), 22481–22515. https://doi.org/10.1364/oe.24.022481

[37] Heatley, D. R., Wright, E. M., Ehrlich, J., & Stegeman, G. I. (1988). Nonlinear directional coupler with a diffusive Kerr-type nonlinearity. *Optics Letters*, *13*(5), 419–421. https://doi.org/10.1364/OL.13.000419

[38] Morimoto, Y., Matsui, H., Hikita, M., & Ishigure, T. (2020). Polarization dependence of optical properties of single-mode polymer optical waveguides fabricated under different processes at 1310/1550 nm. *Journal of Lightwave Technology*, *38*(14), 3670–3676. https://doi.org/10.1109/JLT.2020.2980013

[39] Nawata, H., Oshima, J., & Kashino, T. (2018). Organic-inorganic hybrid material SUNCONNECT® for photonic integrated circuit. In *Optical Interconnects XVIII*, *10538*, 105380F. https://doi.org/10.1117/12.2291308

[40] Abe, K., Oizumi, Y., & Ishigure, T. (2018). Low-loss graded-index polymer crossed optical waveguide with high thermal resistance. *Optics Express*, *26*(4), 4512–4521. https://doi.org/10.1364/oe.26.004512

[41] Gong, Z., Yin, R., Ji, W., Wang, J., Wu, C., Li, X., & Zhang, S. (2017). Optimal design of DC-based polarization beam splitter in lithium niobate on insulator. *Optics Communications*, *396*, 23–27. https://doi.org/10.1016/j.optcom.2017.03.028

[42] Truong, C. D., Nguyen, M. C., Le, D. T., & Le, T. T. (2016). All-optical switch based on 1 × 3 multimode interference couplers. *Optical Switching and Networking*, *22*, 129–134. https://doi.org/10.1016/j.osn.2016.07.002

How to Cite: Alam, M. K., Afsary, N., Islam, M. Z., & Rasel, M. O. F. (2024). Investigation of Polymer-Based 1 × 2 All-Optical Switches at C-Band Wavelength. *Journal of Optics and Photonics Research*, *1*(2), 59–66. https://doi.org/10.47852/bonviewJOPR42022168